

Automatic quantification of the microvascular density on whole slide images, applied to paediatric brain tumours

Christophe Deroulers^{*1}, Volodia Dangouloff-Ros^{2,3}, Mathilde Badoual¹, Pascale Varlet^{3,4,5} and Nathalie Boddaert^{2,3,4,6}

¹Univ Paris Diderot, Laboratoire IMNC, UMR 8165 CNRS, Univ Paris-Sud, F-91405 Orsay, France

²Department of Paediatric Radiology, Hôpital Necker EnfantsMalades, AP-HP, 75105 Paris, France

³INSERM U1000, Paris, France

⁴Univ Paris Descartes, Paris, France

⁵Department of Neuropathology, Centre Hospitalier Sainte-Anne, Paris, France ⁶UMR 1163, Institut Imagine, Paris, France

Email: Christophe Deroulers* - deroulers@imnc.in2p3.fr; Volodia Dangouloff-Ros - volodia.dangouloff-ros@aphp.fr; Mathilde Badoual - badoual@imnc.in2p3.fr; Pascale Varlet - varlet@ch-sainte-anne.fr; Nathalie Boddaert - nathalie.boddaert@aphp.fr;

*Corresponding author

Abstract

Background: Angiogenesis is a key phenomenon for tumour progression, diagnosis and treatment in brain tumours and more generally in oncology. Presently, its precise, direct quantitative assessment can only be done on whole tissue sections immunostained to reveal vascular endothelial cells. But this is a tremendous task for the pathologist and a challenge for the computer since digitised whole tissue sections, whole slide images (WSI), contain typically around ten gigapixels.

Methods: We define and implement an algorithm that determines automatically, on a WSI at objective magnification 40 \times , the regions of tissue, the regions without blur and the regions of large puddles of red blood cells, and constructs the mask of blur-free, significant tissue on the WSI.

Then it calibrates automatically the optical density ratios of the immunostaining of the vessel walls and of the counterstaining, performs a colour deconvolution inside the regions of blur-free tissue, and finds the vessel walls inside these regions by selecting, on the image resulting from the colour deconvolution, zones which satisfy a double-threshold criterion. The two thresholds involved are automatically computed from the WSI so as to cope with variations in staining and digitisation parameters. A mask of vessel wall regions on the WSI is produced.

The density of microvessels is finally computed as the fraction of the area of significant tissue which is occupied by vessel walls.

We apply this algorithm to a set of 186 WSI of paediatric brain tumours from World Health Organisation grades I to IV.

Results: The algorithm and its implementation are able to distinguish on the WSI the significant tissue and the vessel walls. The segmentations are of very good quality although the set of slides is very heterogeneous (in tumour type, in staining and digitisation parameters, and inside WSI themselves, where the tissue was often very fragmented). The computation time is of the order of a fraction of an hour for each WSI even though a modest desktop computer is used (a 2012 Mac mini) and the average size of WSI is 7 gigapixels. The computed microvascular density is found to be robust. We find that it strongly correlates with the tumour grade.

Conclusions: We have introduced a method of automatic segmentation of significant, blur-free tissue and of vessel walls, and of quantification of the density of microvessels, in WSI. We successfully tested it on a large variety of brain tumour tissue samples. This method requires no training and estimates automatically several important parameters of the segmentation. It is robust and can easily be applied to other tumour types and other stainings. It should improve the reproducibility of quantitative estimates in pathology while sparing the pathologist time and effort.

Keywords: Digital Pathology, Image Processing, Whole Slide Images, Angiogenesis, Microvessels, Brain Tumour.

Introduction

Angiogenesis is one of the key features of tumour progression, sustaining growth and sometimes enabling a change of aggressiveness when it starts [1]. In brain tumours [2, 3], it is a crucial histology criterion used in diagnosis and to classify the disease into the proper World Health Organisation (WHO) grade [4]. Therefore, it is of great importance to be able to quantify in a reliable and robust way the status of the tumour vascular system. Although there exist several noninvasive, macroscopic imaging techniques [5–7], not all of them are innocuous (they may use ionising radiations or contrast agents), and they don't yield a direct access to the geometric parameters of the vasculature. In contrast, after proper immunohistochemical staining [8, 9], biopsy samples reveal directly the tumour microvessels. It has been shown that the microvascular density, as measured on histology sections, is of prognostic significance in several brain tumours [10, 11].

However, assessing manually the density of microvessels on whole histology sections is a tremendous task, very hard to perform for a human, and prone to much inter- (and even intra-) individual variability and lack of reproducibility. Quantifying the vascularity only on a few randomly chosen regions, or on a few “representative” regions on the section [12] will make the task easier (shorter) for the pathologist, but will increase the measurement variability and might reinforce the subjectivity of the task.

Luckily, virtual microscopy and the digitisation of pathology slides have become quite common over the last few years, allowing the use of the computer to perform various quantitative and reproducible measurements on histology sections [13]. In the beginning of this digital era, for cost and material reasons, it was not possible to measure the parameters

of microvessels at full resolution (20x or 40x), and it was suggested to use images at resolution around 1x [14, 15]. However, slide scanners produce now high resolution microscopy images of whole slides in a short time (at most a few minutes) and for a reasonable price [16], and using them for quantification should improve the precision of the results. The drawback of this high resolution is the very large size of the resulting files, which require specific software tools to be managed, like the ones some of us have already developed [17–19].

Such a quantification of microvessels on high-resolution images has already been undertaken by several groups [20–22]. However, most of them were limited to small excerpts of the whole slide images (WSI), and possibly to relatively homogeneous sets of slides. Here, we report on a set of techniques we have developed to assess the density of microvessels on WSI of sizes a few tens of gigapixels, immunostained with CD34 (to reveal vascular endothelial cells), within a few minutes, in a robust way, with a careful determination of zones of tissue without blur, and with as little intervention of the pathologist as possible. In particular, no training of an algorithm is necessary, hence the time-consuming task of manual segmentation of a number of vessels to feed to the computer is spared.

Although immunofluorescence is able to provide valuable additional quantitative information about the vasculature, such as 3D aspects [23], it requires the use of more elaborate microscopy and it not yet compatible with clinical routine. Therefore, we stick to classical bright field microscopy of immunostained pathology thin sections.

To demonstrate the versatility and scalability of our method, we applied it to a series of 129 human patients (186 WSI in total) suffering brain tumours of 19 different combinations of histological type and

location, ranging from WHO grade I to grade IV. Since WSI are very large (our largest image had 162688×98816 pixels), they can't be opened in full in a standard computer's memory (we would need up to 60 GiB of RAM), and we had to develop strategies to treat them entirely without restricting ourselves to small excerpts. We used only open source software, or software we developed based on existing open source libraries, to avoid black-box algorithms, to promote interoperability and reproducibility, to reduce costs, and to avoid conflicts of interest [24].

Material and Methods

Our goal is to quantify the density of microvessels on a WSI as the ratio of the area occupied by vascular endothelial cells to the area occupied by the tissue. We assume that the WSI was obtained as a (possibly pyramidal) tiled TIFF or BigTIFF [25] file by digitisation at objective magnification $20\times$ or $40\times$ of a $5\mu\text{m}$ -thick tissue section of formalin-fixed, paraffin-embedded tissue, and that immunostaining with a CD34 antibody was performed so that microvessels appear brown whereas cell nuclei appear blue. The total area of tissue is typically of a few square centimetres.

If some deviation from this protocol is in order, it should be easy to adapt our method. E.g., if the WSI is stored in another format, it can be converted to TIFF using the free software NDPITools [17,19] that we developed or OpenSlide [26,27]. If the colours after immunostaining are different, two parameters can be changed (see below).

Method overview

The aim is first to select the zone of tissue on the WSI, then the zone of vessel walls inside the zone of tissue, and finally to measure the areas of the two and compute their ratio. Because of unavoidable slide-to-slide variations in staining and digitisation parameters (e.g. light intensity or temperature colour), both zone selections will require prior calibration steps. And, due to technical details, the work flow will be slightly more complex. We must:

- exclude from the WSI regions where the image is not sharp enough to recognise vessel walls accurately
- exclude from the WSI regions which look like tissue but should not be counted as such: es-

entially large puddles of red blood cells, coverslip boundaries and dust

- not count as vessel walls extra-vascular CD34-positive tumour cells.

A scheme of the whole process is shown in Figure 1.

Preparatory steps

From the full-resolution $40\times$ image, a $20\times$ image was generated by bilinear interpolation and stored into a JPEG-compressed [28] tiled TIFF [29] file. Indeed, such an image proved of sufficient quality for several of the steps below while saving computation time.

Then, a mosaic of the $20\times$ image was made and stored into JPEG files. This is a decomposition of the original image in rectangular pieces of equal sizes, stored into independent files for easy independent treatment, such that the original image is recovered if the pieces are reassembled together. We requested that each piece need at most 128 MiB to be stored (uncompressed) in RAM and that the dimensions of each piece be multiples of 8 pixels. This can be easily achieved using the `-m` and `-M` options of the `tiffmakemosaic` software [17,19].

Selection of sufficiently sharp zones

We used a variation of the method of blur quantification of [30,31]. On each piece of the $20\times$ mosaic, after decompression into RGB colour space, we applied a colour space transformation into HSV colour space as defined by the `vips` program [32], extracted the V channel and convoluted the resulting image with the Laplacian kernel

$$\begin{pmatrix} -1 & -1 & -1 \\ -1 & 8 & -1 \\ -1 & -1 & -1 \end{pmatrix}.$$

Then, considering the result of the convolution as a mosaic of blocks of 8×8 pixels, we computed the S_2 score [31], namely the ratio of the sum of pixel intensities which are at least 10% of the maximum intensity in the block to the sum of all 64 pixel intensities (or 0 if the denominator is vanishing). Such a division into blocks of 8×8 pixels is natural since it is at the basis of the JPEG compression used by most slide scanners and used by our method to store the $20\times$ image while saving disk space; artefacts due

to this blocking are already present in the original WSI.

We generated a graylevel image where the S_2 value of each block of the $20\times$ image was encoded as the intensity of one pixel (between 0 and 255 included). The resulting image, which can be deemed a sharpness map, is 16 times smaller (in linear dimension) than the original $40\times$ image, thus has 256 times less pixels, and could easily be stored in a single file and opened at once in the computer’s RAM.

Finally, this $2.5\times$ sharpness map was transformed (using the ImageJ software [33, 34]) into a mask of sharp regions in the following way: pixel intensities were averaged over regions of radius 2 pixels; a mask of regions where the resulting intensity is 43 and above was created (these are the sharp regions); sharp regions of less than 20 pixels of area (at resolution $2.5\times$) were turned into blurred regions, then blurred regions of less than 20 pixels of area were turned into sharp regions. The final mask of sharp regions was written on the disk.

Selection of tissue zones

We used as a first criterion to distinguish tissue from background the value of brightness of pixels (B in HSB colour space as defined by ImageJ [33]). Therefore, we needed to calibrate the brightness of pixels in the background.

This calibration may be influenced by the sides of the coverslip (and zones beyond) which are visible on 10 of our WSI. For each of these few images, we manually contoured the side of the coverslip on a downsampled $0.625\times$ image and stored the resulting contour (union of polygons) as ImageJ’s `roi` files which will be subsequently read at the proper stage.

We generated a $2.5\times$ image from the full resolution image. With ImageJ, we selected on this image the non-excluded zones (sides of the coverslip), then we extracted the brightness of pixels (between 0 and 255) and selected pixels the brightness of which differed by less than ± 1.2 from the Gaussian-weighted average (with standard deviation $\sigma = 0.005$) over their vicinity. We selected connected regions of at least 160 pixels among these “uniform” pixels and took the intersection with regions where the brightness was 127 or above. This defined the reference regions for the background.

We measured the histogram of the brightness value of the pixels in the reference regions. It always exhibits a peak of occurrence numbers of levels be-

tween 200 and 255. We measured the right end $b_{bg,r}$ of this peak, as the largest brightness level which occurs at least once. Then we measured the left end $b_{bg,l}$ of this peak using the following algorithm: starting from the right end, we scanned occurrence numbers of decreasing brightness levels. We stopped when the current occurrence number was below half of the largest observed occurrence number so far and either was zero or was larger than the last seen occurrence number.

These left- and right-end define rather accurately the brightness of pixels belonging to the background and we stored them in a text file for later reuse. They had to be determined for each WSI because of marked variability: the left-end ranged from 212 to 234 while the right-end ranged from 232 to 249.

In addition, we selected pixels within the reference regions which had a brightness between the left-end of the peak and the left-end plus three (included) and computed their average values of R, G and B (hereafter called R_{bg} , G_{bg} , B_{bg}). We stored these values in a text file for later use.

The actual selection of tissue zones was performed on pieces of a mosaic of the image at resolution $20\times$. We produced with `tiffmakemosaic` a mosaic such that no piece required more than 100 MiB of RAM to be opened, with overlap of 256 pixels between adjacent pieces. Pieces were stored as TIFF files with zip compression (rather than JPEG compression to avoid another information loss and to facilitate opening by ImageJ). On each piece, ImageJ was used to produce a mask of the tissue zones in the following way. We selected the pixels the brightness of which was outside the interval measured previously as “background intensity peak”, $[b_{bg,l}, b_{bg,r}]$ — call them A-pixels. Then, among the connected regions formed by these pixels, we selected those which contained at least one pixel the saturation of which (in HSB space) was larger than the average of the saturation of all A-pixels — thus constructing the B-regions. This was to prevent selecting uniform regions with unusual high or low brightness, which could be a large piece of dust or a pen stroke (uniformly black region).

The resulting regions could contain “holes”, some of which were regions of background inside a region of tissue. We noticed that almost all holes of less than ≈ 10000 pixels (at $20\times$ magnification) had to be considered as tissue. Therefore, we included in the B-regions the holes of area less than 10000 pixels and which did not touch the boundaries of the mosaic

piece. Indeed, a hole touching a boundary either was a small part of a bigger hole (more than 10000 pixels) extending on another mosaic piece, which should not be restored into the B-regions, or a small part of a small hole which would quite probably be entirely included into an adjacent mosaic piece, because mosaic pieces overlapped by 256 pixels. The exception would concern only small holes (less than 10000 pixels), a dimension of which exceeded 256 pixels, that is rather elongated holes, which was rather uncommon.

Similarly, we found that holes having a fractal-like shape should also be restored as tissue in the B-regions. They were characterised in the following way: after we performed an `erode` then a `dilate` operation on them, their area was less than 10000 pixels, and they did not touch the boundary of the mosaic piece.

Then we made the boundaries of the B-regions (tissue regions) more regular applying an `erode` then a `dilate` on their mask. This eliminated the small overhangs or invaginations of a few pixels.

We eliminated from the B-regions the connected regions of less than 20000 pixels which were at a distance 30 pixels or larger from a region or 20000 pixels or more. Indeed, most of those were found to be non significant (dust, isolated cells, small pieces of tissue torn apart). And in the end we are interested only in the fraction of tissue area covered by vessels, which we neither overestimate nor underestimate by mistakenly removing a small significant area of tissue. This last operation was performed in ImageJ by a combination of morphological operations, including thresholding at 15 the distance map from the B-regions.

Finally, we found that B-regions with too low saturation (greyish regions) could exist and should be disregarded as tissue (tissue contains at least blue cell nuclei or brown vessel walls). Therefore, after convoluting by a Gaussian kernel of standard deviation $\sigma = 3$ pixels the image of the saturation in HSB colour space, we applied the isodata algorithm [35] to find an automatic threshold on this image and we defined as high-saturation pixels the pixels the saturation of which was above the isodata threshold and above 30. Only B-regions containing at least one high-saturation pixel were kept as tissue regions.

The mask (binary image) of the tissue regions of each mosaic piece was saved as PNG files, then all PNG files were combined into a large, $20\times$ resolution, mask of tissue thanks to an in-house developed

C program for the sake of speed and RAM economy. The whole mask was stored on the disk as a 1-bit-per-pixel Deflate-compressed [29] TIFF file, which achieves a very high level of compression. Then the pieces of the mosaic with overlap were erased from the disk.

If there existed, for this WSI, a `.roi` file defining the side(s) of the coverslip on the image, the mask of the region to exclude was formed as a binary image of resolution $0.625\times$ and the mask of tissue was replaced by the result of a logical `and` of the former mask of the tissue and the inverse of the mask of the region to exclude blown up to resolution $20\times$. This logical operation was performed thanks to another in-house developed C program, again for the sake of speed and RAM economy.

Finally, the logical `and` of the mask of sharp regions and of the mask of tissue was computed through the same C program and stored on the disk as a bilevel, Deflate-compressed TIFF file. Again, although the resulting mask is a very large image (1,76 gigapixels in average), this form of compression is very efficient: the average disk size of the mask was 4,36 MiB, ranging from 0,26 MiB to 16,38 MiB.

A detail from an example of such a mask of sharp tissue is shown, superimposed onto the corresponding WSI, in Figure 2.

Removal of puddles of red blood cells

This part of the method is rather cumbersome and empirical, but we found it useful since, on several WSI of brain tumours, the puddles of red blood cells occupied more than 30% of the regions of blur-free tissue. It was developed on two example WSI but proved efficient on all.

We constructed a mask of large puddles of red blood cells on the WSI at objective magnification $40\times$ in the following way. We changed the colour space to HSB (as defined in ImageJ) and operated on the B channel.

First (step 1), on the result of the contour detection (application of a 3×3 Sobel filter, ImageJ's `Find Edges` command), we selected connected regions of at least 20 pixels at levels 250 and above, and pixels at the distance at most 10 pixels from these regions, then retained, from these enlarged connected regions, only those which had at least 10,000 pixels.

Second (step 2), we selected pixels of brightness exactly 255 and performed a morphological `close` operation on the resulting mask. This is to select

the sides of the red blood cells, which appear very bright in bright field microscopy (because of the refringence property of these cells) and elongated (because of the circular shape of these cells). We skeletonised the result and eliminated the connected regions of at most 9 pixels. Then we extended the remaining skeletons to pixels within the distance of 20 pixels and eliminated the connected regions of less than 20,000 pixels. Defining the threshold $b := 255 - 0.35(255 - b_{bg,r})$, where $b_{bg,r}$ was defined during background's brightness calibration (see above), we retained, among the remaining regions, only those which contained at least one connected regions of 40 pixels or more with brightness above b and of circularity at most 0.2. We also added the connected regions of 2800 pixels and above which were constructed by added to these latter regions pixels at distance at most 2800.

We took the union of the regions defined in the two preceding steps (1 and 2). We added the pixels at distance at most 20 pixels of these regions and inside the convex hull of at least one of these regions. This formed a mask of puddles of red blood cells. Finally, we added to the mask the holes of less than 100,000 pixels if contained, and stored the mask on the disk as a 1-bit-per-pixel Deflate-compressed tiled TIFF image as before.

A detail from an example of such a mask of large puddles of red blood cells is shown, superimposed onto the corresponding WSI, in Figure 3.

Removing from the mask of sharp tissue pixels considered, according to this mask of puddles of red blood cells, we built the mask of significant, blur-free tissue.

Calibration of optical density ratios of stains

Since the vascular endothelial cells were marked with a brown staining over a blue counterstaining, information relevant to the microvessels are be entirely contained in the brown channel after we perform a colour deconvolution [36].

To perform this linear change in colour space, we needed to know the optical densities (o.d.) in R, G and B channels (or, more precisely, only the ratios of these three o.d. to form their vector in the RGB space [36]) of the two stains, brown and blue. We couldn't use standard values from the literature nor common values for all WSI since, as for the brightness of the background above, there was a strong slide-to-slide variability, as can be seen on Figure 4.

We used the following procedure on each piece of the $20\times$ mosaic without overlap formed earlier. Using ImageJ, we performed a change of colour space to HSB. On one hand, we selected pixels with brightness at most 198, saturation at least 70 and hue outside the interval $[80, 199]$. Among them, we kept only connected regions of at least 25 pixels. Finally, we measured the average optical densities in the R, G, and B channels of these pixels and the number of remaining pixels and wrote these numbers to a text file. This gave the contribution of markedly brown areas. On the other hand, we repeated the procedure with pixels, the saturation of which was at least 70 and with hue inside the interval $[80, 199]$ to get the contribution of markedly blue areas.

Then we aggregated the results from all mosaic pieces to compute the average over the whole slide of the optical densities in R, G, and B channels of the brown and blue stains and wrote them to a text file.

The precise values of the thresholds above are irrelevant: the important thing is that the loose limits on the hue 80 and 199 clearly separate brown from blue (they can of course be adapted to other colours) and that the loose limits on the saturation and brightness select as representative areas for calibration regions markedly brown resp. blue. In average, the calibration of the optical densities of the brown staining rested on 15,4 megapixels (min: 56,3 kilopixels, max: 288 megapixels) and the calibration of the optical densities of the blue rested on 104 megapixels (min: 1,09 megapixels, max: 842 megapixels).

Selection of vessel walls

The whole process of actual selection of vessel walls operated only on the areas of significant, blur-free (sharp) tissue of the WSI, which were indicated by the mask constructed earlier.

First, the histogram H_B of the brown optical density (o.d.) of each pixel after colour deconvolution was constructed. This was achieved through an in-house developed C program which took as input the WSI at resolution $20\times$, the mask of sharp tissue and the parameters of the colour deconvolution (average o.d. determined earlier) and operated independently on each tile of the WSI to save RAM and allow the use of parallel processing on a computer with multicore CPUs. Here, the restriction to areas of sharp tissue also avoided to bias the histogram

with values from irrelevant pixels (e.g. dust).

Then, a global (but WSI-specific) threshold on the brown o.d. for vessel walls on the WSI, hereafter called b_A , was automatically determined from the histogram in the following way. First, we computed b_{bg} , the brown o.d. of a pixel with colour (R_{bg}, G_{bg}, B_{bg}) stored earlier (average colour of the darkest pixels of the background reference regions). Then, we applied the `isodata` automatic method of threshold computation [35] on the part of the histogram H_B concerning o.d. above b_{bg} .

We could not rely on the full histogram to determine b_A since, on some of the WSI, cell nuclei were so dense in the tissue that they would manifest themselves as a peak in the low o.d. region of the histogram H_B , so that the value b_1 computed by the `isodata` algorithm would be influenced by them instead on yielding information on the vessel walls only. Disregarding the low o.d. values of brown, that is, o.d. values below those of the background, was a simple and efficient way to solve this problem.

Then, a second global (but also WSI-dependent) threshold, called b_B , was computed by a new application of the `isodata` algorithm on the part of the histogram H_B concerning o.d. above b_A .

The actual segmentation of the vessel walls consisted essentially in looking for connected sets of pixels, inside the sharp tissue, which had brown o.d. above (or equal to) b_A and which contained at least a small regions where brown o.d. was above (or equal to) b_B . The second condition avoided that pale brown regions be inaccurately recognised as vessel walls (this concerned for instance a few isolated CD34-positive tumour cells).

This was performed by treating in turn each rectangular zone of size roughly 3840×3840 of the WSI at resolution $20\times$. The zone was extracted using the `tiffcrop` program from the `LargeTIFFTools` [17, 18] (which can extract very quickly a rectangular zone from a (possibly huge) tiled TIFF image, twice as fast as the `extract_area` command of `vips`). The corresponding zone from the mask of sharp tissue was extracted. Then an ImageJ macro selected pixels from the extract of the WSI inside the sharp tissue zones according to the mask, performed colour deconvolution and created a mask of the brown o.d. of pixels which satisfy one of the three conditions: the brown o.d. is above (or equal to) b_A , the brightness (in HSB colour space) is at most 30, or the brightness is at most 40 and the saturation at most 127. The two latter conditions

were necessary because almost black pixels composing some of the vessel walls may have low values of brown o.d. (as already noticed for brown staining [36]) and may be missed by the first condition.

The mask was post-processed in the following way. Let us call A-regions the connected regions of pixels selected so far on the basis of b_A (discarding regions of less than 75 pixels). We convoluted the image of brown o.d. with a Gaussian kernel of standard deviation 0.5 pixel, then kept pixels with intensity b_B and above, then connected regions of at least 25 pixels of these pixels. Finally, we kept as vessel walls in the current rectangular zone the A-regions containing at least a B-region. We recorded their mask on the disk as a PNG file.

As in an earlier step, we used our C program to merge all masks of vessel walls in rectangular zones into a single mask at $20\times$ resolution stored in a bilevel, Deflate-compressed tiled TIFF file, where vessel walls were black and the background was white.

Review of the segmentation results

For each slide, we produced a set of files in DeepZoom format from the WSI at resolution $40\times$ using `vips`. We also produced sets of files in DeepZoom format for the mask of sharp tissue and the mask of vessel walls. And we produced in DeepZoom format the image of the contours of vessel walls, where all pixels are transparent, except the pixels which belong to a boundary of a vessel wall (black pixels surrounded by at least one white pixel).

These sets of files were uploaded to a secured web server, along with a simple HTML file (automatically generated by a simple Perl script) calling the JavaScript OpenSeadragon [37] library to display the superimposition of the slide and, according to what the user selects, of the different masks or contours.

This allowed a convenient quality control of the segmentation of tissue and vessels by the pathologist from his office or a meeting room at the Hospital, even though the whole image processing was performed on a computer in a physics laboratory. Indeed, all that was needed for this visualisation was a standard desktop computer with a JavaScript capable web browser. A typical session of quality check is displayed on Figure 6.

Material of our cohort

We applied our method to a cohort of 129 human patients suffering from brain tumours ranging from WHO grade I to grade IV and in various locations: posterior fossa, thalamus and hemispheres. The detailed numbers are given in Table 1. Such a variety of tumour types served as a challenge to our method (see if it is really robust even without human intervention) and was also meant to check how much the microvascular density was correlated with tumour grade.

Each sample was prepared the same way: a $5\mu\text{m}$ -thick tissue section of formalin-fixed, paraffin-embedded tissue was immunostained with a monoclonal mouse anti-human CD34 antibody (QBend-10, Dako®, Agilent Technologies, Santa Clara, California, USA). The reaction was carried out in an automated immunohistochemistry instrument (Benchmark, Ventana Medical Systems®, Hoffman La Roche, Basel, Switzerland). Patients were excluded if the pathological sample was insufficient to perform CD34 immunohistochemical analysis.

The resulting 186 tissue sections mounted on glass slides were digitised by a Hamamatsu NanoZoomer at objective resolution $40\times$, which produced a NDPI file per slide. The average size of the files was 748.5 MiB (max: 2.54 GiB), representing in total ≈ 100 GiB of compressed data. The average size of the images was 7.03 gigapixels (max: 16.08 gigapixels).

Results

Quality of the segmentation

The quality of the segmentation was reviewed during a collective meeting in the hospital (involving pathologist, radiologists and physicists). Each slide was displayed thanks to an overhead projector connected to a computer, itself using a web browser to retrieve images from our web server. Out of the 186 slides, 30 had unfortunately to be excluded because they displayed extensive areas of extra-vascular CD34-positive cells.

On a few other slides, the pathologist was able to select zones free from extra-vascular CD34 signal. These zones were defined using ImageJ as unions of polygons on the $2.5\times$ resolution versions of the WSI and stored on the disk as ImageJ's `.roi` files. The corresponding slides were reprocessed by disregarding all pixels outside the selected zones for tissue and

vessel wall selection.

On two other slides, it proved sufficient to manually raise slightly the threshold b_A and to reprocess the slide (vessel selection step) to prevent selecting most extra-vascular CD34-positive cells.

Otherwise, the segmentation was judged of very good quality by the pathologist. An example of the complete segmentation is shown in Figure 5.

Density of microvessels

On each WSI, we counted the number of selected pixels on the mask of sharp tissue and on the mask of vessel walls, and we took the ratio to get the density of microvessels. The measurements were done by an in-house C program for the sake of speed and RAM economy, again treating images tile-wise to enable multicore parallel processing.

The distribution (histogram) of the densities is displayed in Figure 7. We find that it is remarkably correlated with the tumour grade.

Computation time performance

All processing of the WSI was done on a Mac mini computer with 16 GiB of RAM and a quad-core i7 CPU at 2.3 GHz bought in October 2012. Although this computer was rather modest in regard of today's standards, we found the overall treatment time to be quite acceptable.

Figure 8 shows the distribution of the computing time of the vessel wall segmentation (including colour deconvolution), which is one of the most time-consuming operations. One can see that most WSI could be treated in less than 15 minutes. This has to be compared to the time necessary to transfer to the web server the OpenSeadragon files of the WSI and of the masks: the latter was larger even using a large bandwidth network connection.

Let us also notice that selecting the vessel walls only in the areas of sharp tissue of the WSI saved a substantial amount of computation time, since the average fraction of the WSI occupied by the sharp tissue was only 26.8% (ranging from 1.9% to 63.6%). Most of the rest of the WSI was usually background, empty space.

Discussion

Inter-slide variability and robustness

As we already discussed, several of the physical parameters of the WSI (colour temperature of the background, optical densities of the stains,...) vary largely from one slide to the next. This is why our method includes several steps of calibration. Some previous studies [22] used values of the parameters of the segmentation common to all slides, but this was for smaller sets of slides. In our heterogeneous set of 186 slides, this would yield wrong results. For instance, the thresholds b_A resp. b_B on brown o.d. for vessel segmentation have the following statistics: average 93.2, min. 44, max. 160 resp. average 178.5, min. 159, max. 250.

We believe that other parameters (parameters which were not chosen after a calibration) fall in two categories: parameters, the value of which is not very relevant, and parameters which might influence the final result of the WSI. In the first category fall e.g. the precise limits of the interval of hue used to define the reference areas for the calibration of brown and blue optical densities. Changing these limits will alter only very marginally (if at all) the measured o.d., hence the vessel segmentation. It is therefore not worth to give too much attention to them.

Parameters in the second category include e.g. the threshold used to fix the limit between sharp and blurred tissue, and most of the geometrical parameters of the segmentation of tissue (the minimal / maximal number of pixels of connected regions to be kept / disregarded, the maximal distance of a small piece of tissue to a large piece to be considered as significant,...). We did only a manual calibration of them, based on a representative set of a few slides or a few excerpts of slides. But, even if a different choice for their value could change the final measured microvessel density, we think that this change is less important than in the case of calibrated parameters (like stains' o.d.) and that it would be systematic, affecting the measure roughly in the same way on all WSI. Hence fixing these values doesn't preclude the use of our automatic measurement for assistance to tumour grading.

Finally, let us remark that, even with these possible limitations in mind, our method should be much more reproducible than manual measurements performed on a few chosen excerpts in each slide even by a trained pathologist [15], if the latter is at all doable on such a large set of slides. We prefer to save

the pathologist's time for quality control and make our overall study cheaper by the extensive use of the computer. Notice also that, among our 186 slides, many have very fragmented tissue (all the more that we are dealing with fragile brain tissue), making it very difficult to estimate accurately the area of tissue. And, of course, a systematic manual vessel segmentation is not in order: there is an average of 16571 vessel fragments in the sharp tissue area of our slides (min. 58, max. 72614).

Impact of red blood cells

The fraction of blur-free tissue occupied by puddles of red blood cells, as determined by the method above, ranged from 0.04% to 37.2%. In average, such spreads of red blood cells occupied 4.87% of the blur-free tissue, so they were not a crucial issue for the determination of the microvascular density for most slides. But for 8 of our 186 slides they occupied more than 25% of the apparent tissue, and for 21 of them they occupied more than 10% of the apparent tissue. For these slides, had we counted the puddles of red blood cells as tissue, we would have underestimated the density of microvessels by 10 to 25%, which is huge in comparison, e.g., to the difference of microvascular density between low-grade and high-grade tumours (Figure 7).

Therefore, we believe that the step of automatic detection of puddles of red blood cells, although cumbersome and time-consuming, is necessary. We couldn't save time by performing it on the 10× magnification WSI instead of the 40× WSI because the specifically high intensity pixels of the red blood cells' sides (due to their refringence) was lost during the resolution reduction.

Uncertainties

We tried to assess the uncertainties on the measurement of the microvessel density against the most important parameters of the method in the following way.

- Changing by one (over 255) the brown o.d. threshold b_A changed by 0.5% the total area of the regions recognised as vessel walls. Therefore, the uncertainty on b_A and b_B , as determined automatically by a thresholding algorithm [35] up to a few units over 255, has little influence on the final result. But remem-

ber, once again, that this automatic threshold varies strongly from one slide to the next one: the standard deviation on b_A is 21.1.

- Eroding or dilating either the regions recognised as vessel walls or the regions recognised as tissue by one pixel at resolution $20\times$ changed by $\approx 7\%$ the area. This is more serious and means that one has little latitude on morphological post-processing of the segmented regions. However, a change by 7% is still acceptable if one wants to use the microvessel density to distinguish between low-grade and high-grade tumours, owing to the large spreading of the density (see Figure 7). It should be interesting to redo the measurement using the WSI at magnification $40\times$ and see if the uncertainty against eroding or dilating is smaller as one could expect, at the expense of a computation time four times larger.

In a context of strongly heterogeneous tissue, measuring the microvessel density on whole tissue sections also contributes to reduce the uncertainties by allowing the measurement to rest on a large zone of tumour tissue, hence reducing the risk to measure accidentally a zone with especially low or high vessel density.

Additionally, if one wants to draw a link between measurements at the microscopic scale (on WSI) where individual cells are resolved, and at macroscopic scale (using e.g. MRI) where the resolution is routinely of the order of 1 mm, one has to perform the microvessel density measurement on the largest (but still relevant) piece of tissue. In this spirit, and to further confirm the quality and relevance of our measurement on brain tumour tissues, it has been shown that the microvascular density we measured is in good correlation with the result of a noninvasive, macroscopic measurement using the ASL modality of MRI [11].

Further development

We plan to extend this work in several directions. First of all, the overall process can still be optimised to reduce the treatment time of each slide.

Then, much information is still left unexploited: on one hand, we plan to perform morphometry analyses on the segmented vessel walls [20, 22, 38]. This could serve as a basis for a system of computer aided diagnosis of some of the tumours. And this

would yield precious data to develop a theoretical model of angiogenesis in brain tumours, which hopefully could guide treatments in the long term, in the spirit of what is being done e.g. for adult low-grade gliomas [39].

On the other hand, no information about cell nuclei has been exploited yet. It should be relatively easy to perform segmentation on e.g. the blue channel after colour deconvolution and get quantitative parameters in the same way as for vessels: density of nuclei, morphometry...

And, beyond morphometry on the black-and-white masks resulting from the mere segmentation (thresholding) of biological objects, it could also be possible to extract more information from the virtual slides by continuously varying the threshold defining A-regions. In this way, a series of segmentations is built and can be analysed as would be a time series [40], revealing more aspects of the disease than a static picture taken at a single time point.

Finally, angiogenesis has been shown to be of significant value for diagnosis and prognostic more generally in oncology [41–43], so that our method can readily be applied to other tumours with the same of similar immunostainings (CD31, CD34).

Conclusions

We have introduced an automatic and training-free method of quantification of the density of microvessels on whole tissue sections immunostained with the CD34 antibody and digitised by a slide scanner. This method is, to our knowledge, the first one to include a careful determination of areas of tissue without blur and puddles of red blood cells before the proper segmentation of vessel walls.

We tested in on a large set of WSI (186) of a very large variety of brain tumours. Using a very reasonable amount of computation time on a quite affordable computer system (an Intel Core i7 CPU with 16 MiB of RAM), this method produced results of very good quality, even though an overall check of the segmented WSI by the pathologist was necessary, in particular because of extra-vascular CD34-positive tumour cells. It should be helpful in computer-aided diagnosis systems and easily reused for other stainings/tumours, especially because it uses only open source software (like ImageJ or vips) or well-described algorithms, and because its architecture is simple and modular and its parameters

easy to understand and modify (e.g. to adapt it to other colours than brown and blue).

Competing interests

The authors declare that they have no competing interests.

Acknowledgements

We thank the CNRS/IN2P3 computing centre for hosting the website we used to view WSI and control the quality of segmentation.

CD and MB belong to the CNRS consortium CellTiss and to the Labex P2IO.

References

1. Carmeliet P, Jain RK: **Angiogenesis in cancer and other diseases.** *Nature* 2000, **407**(6801):249–57.
2. Onishi M, Ichikawa T, Kurozumi K, Date I: **Angiogenesis and invasion in glioma.** *Brain Tumor Pathol* 2011, **28**:13–24.
3. Plate KH, Scholz A, Dumont DJ: **Tumor angiogenesis and anti-angiogenic therapy in malignant gliomas revisited.** *Acta Neuropathologica* 2012, **124**(6):763–75.
4. Louis DN, Perry A, Reifenberger G, von Deimling A, Figarella-Branger D, Cavenee WK, Ohgaki H, Wiestler OD, Kleihues P, Ellison DW: **The 2016 World Health Organization Classification of Tumors of the Central Nervous System: a summary.** *Acta Neuropathologica* 2016, **131**(6):803–820, [<http://dx.doi.org/10.1007/s00401-016-1545-1>].
5. Sun H, Xu Y, Yang Q, Wang W: **Assessment of Tumor Grade and Angiogenesis in Colorectal Cancer: Whole-volume Perfusion CT.** *Academic Radiology* 2014, **21**(6):750–757.
6. Cha S, Knopp EA, Johnson G, Wetzel SG, Litt AW, Zagzag D: **Intracranial Mass Lesions: Dynamic Contrast-enhanced Susceptibility-weighted Echo-planar Perfusion MR Imaging.** *Radiology* 2002, **223**:11–29.
7. Peet AC, Arvanitis TN, Leach MO, Waldman AD: **Functional imaging in adult and paediatric brain tumours.** *Nat Rev Clin Oncol* 2012, **9**:700–11.
8. Parums DV, Cordell JL, Micklem K, Heryet AR, Gatter KC, Mason DY: **JC70: a new monoclonal antibody that detects vascular endothelium associated antigen on routinely processed tissue sections.** *J. Clin. Pathol.* 1990, **43**(9):752–757.
9. Fina L, Molgaard H, Robertson D, Bradley N, Monaghan P, Delia D, Sutherland D, Baker M, Greaves M: **Expression of the CD34 gene in vascular endothelial cells.** *Blood* 1990, **75**(12):2417–2426.
10. Folkerth RD: **Descriptive analysis and quantification of angiogenesis in human brain tumors.** *J. Neurooncol.* 2000, **50**:165–72.
11. Dangouloff-Ros V, Deroulers C, Foissac F, Badoual M, Shotar E, Grévent D, Calmon R, Pagès M, Grill J, Dufour C, Blauwblomme T, Puget S, Zerah M, Sainte-Rose C, Brunelle F, Varlet P, Boddart N: **Arterial Spin Labeling to predict brain tumor grading in children: Correlations between histopathologic vascular density and perfusion MR Imaging.** *Radiology* 2016, **281**.
12. Kayser K, Nwoye JO, Kosjerina Z, Goldmann T, Vollmer E, Kaltner H, André S, Gabius HJ: **Atypical adenomatous hyperplasia of lung: its incidence and analysis of clinical, glycohistochemical and structural features including newly defined growth regulators and vascularization.** *Lung Cancer* 2003, **42**:171–182.
13. Gürcan MN, Boucheron LE, Can A, Madabhushi A, Rajpoot NM, Yener B: **Histopathological Image Analysis: A Review.** *Biomedical Engineering, IEEE Reviews in* 2009, **2**:147–171.
14. Kim NT, Elie N, Plancoulaine B, Herlin P, Coster M: **An Original Approach for Quantification of Blood Vessels on the Whole Tumour Section.** *Anal. Cell. Pathol.* 2003, **25**(2):63–75.
15. Françoise R, Michels JJ, Plancoulaine B, Herlin P: **Optimal resolution for automatic quantification of blood vessels on digitized images of the whole cancer section.** *Image Anal Stereol* 2005, **24**:59–67.
16. Diamond J, McCleary D: **Virtual Microscopy.** In *Advanced techniques in diagnostic cellular pathology.* Edited by Hannon-Fletcher M, Maxwell P, Chichester, UK: John Wiley & Sons, Ltd 2009.
17. Deroulers C, Ameisen D, Badoual M, Gerin C, Granier A, Lartaud M: **Analyzing huge pathology images with open source software.** *Diagn. Pathol.* 2013, **8**:92, [<http://dx.doi.org/10.1186/1746-1596-8-92>].
18. Deroulers C: **LargeTIFFTools** 2013–2016, [<http://www.imnc.in2p3.fr/pagesperso/deroulers/software/largetifftools/>].
19. Deroulers C: **NDPITools** 2011–2016, [<http://www.imnc.in2p3.fr/pagesperso/deroulers/software/ndpitools/>].
20. Reyes-Aldasoro C, Williams L, Akerman S, Kanthou C, Tozer G: **An automatic algorithm for the segmentation and morphological analysis of microvessels in immunostained histological tumour sections.** *J. Microsc.* 2011, **242**(3):262–278.
21. Niazi MKK, Hemminger J, Kurt H, Lozanski G, Gürcan MN: **Grading Vascularity from Histopathological Images based on Traveling Salesman Distance and Vessel Size.** In *Proc. SPIE, Volume 9041* 2014:90410C–90410C–7, [<http://dx.doi.org/10.1117/12.2043808>].
22. Fernández-Carrobles MM, Tadeo I, Noguera R, García-Rojo M, Déniz O, Salido J, Bueno G: **A morphometric tool applied to angiogenesis research based on vessel segmentation.** *Diagn. Pathol.* 2013, **8**(Suppl 1):S20, [<http://www.diagnosticpathology.org/content/8/S1/S20>].
23. Morin K, Carlson P, Tranquillo R: **Automated image analysis programs for the quantification of microvascular network characteristics.** *Methods* 2015, **84**:76–83.

24. Kayser K: **Introduction of virtual microscopy in routine surgical pathology — a hypothesis and personal view from Europe.** *Diagnostic pathology* 2012, **7**:48.
25. **BigTIFF Design** 2012, [<http://www.remotesensing.org/libtiff/bigtifftiffdesign.html>].
26. Goode A, Satyanarayanan M: **A Vendor-Neutral Library and Viewer for Whole-Slide Images.** Tech. Rep. Technical Report CMU-CS-08-136, Computer Science Department, Carnegie Mellon University 2008, [<http://reports-archive.adm.cs.cmu.edu/anon/2008/CMU-CS-08-136.pdf>].
27. Goode A, Gilbert B, Harkes J, Jukic D, Satyanarayanan M: **OpenSlide: A Vendor-Neutral Software Foundation for Digital Pathology.** *J. Pathol. Inform.* 2013, **4**:27.
28. Lane TG, Vollbeding G: **The Independent JPEG Group's JPEG software** 2013, [<http://www.ijg.org/>].
29. Sam Leffler S, the authors of LibTIFF: **LibTIFF – TIFF Library and Utilities** 2012, [<http://www.remotesensing.org/libtiff/>].
30. Ameisen D, Deroulers C, Perrier V, Yunès JB, Battistella M, Bouhidel F, Legrès L, Janin A, Bertheau P: **Stack or Trash? Quality assessment of virtual slides.** *Diagnostic Pathology* 2013, **8**(Suppl 1):S23.
31. Ameisen D: **Intégration des lames virtuelles dans le dossier patient électronique.** *PhD thesis*, Univ Paris Diderot-Paris 7 2013.
32. Martinez K, Cupitt J: **VIPS - a highly tuned image processing software architecture.** In *Proc. IEEE International Conference on Image Processing 2* 2005:574–577.
33. Rasband WS: **ImageJ** 1997–2016, [<http://imagej.nih.gov/ij/>].
34. Schneider CA, Rasband WS, Eliceiri KW: **NIH Image to ImageJ: 25 years of image analysis.** *Nature Methods* 2012, **9**:671–675.
35. Ridler TW, Calvard S: **Picture Thresholding Using an Iterative Selection Method.** *IEEE Transactions on Systems, Man, and Cybernetics* 1978, **8**(8):630–632.
36. Ruifrok A, Johnston D: **Quantification of Histochemical Staining by Color Deconvolution.** *Anal. Quant. Cyt. Hist.* 2001, **23**:291–299.
37. CodePlex Foundation, OpenSeadragon contributors: **OpenSeadragon** 2015, [<http://openseadragon.github.io/>].
38. Sharma H, Zerbe N, Lohmann S, Kayser K, Hellwich O, Hufnagl P: **A review of graph-based methods for image analysis in digital histopathology.** *Diagnostic Pathology* 2016, **1**:61.
39. Badoual M, Gerin C, Deroulers C, Grammaticos B, Litjos JF, Oppenheim C, Varlet P, Pallud J: **Oedema-based model for diffuse low-grade gliomas: application to clinical cases under radiotherapy.** *Cell Proliferation* 2014, **47**(4):369–380, [<http://dx.doi.org/10.1111/cpr.12114>].
40. Kayser K, Borkenfeld S, Carvalho R, Djenouni A, Kayser G: **How to analyze Structure and Function in Tissue - based Diagnosis?** *Diagnostic Pathology* 2016, **2**:106.
41. Labiche A, Elie N, Herlin P, Denoux Y, Crouet H, Heutte N, Joly F, Héron JF, Gauduchon P, Henry-Amar M: **Prognostic significance of tumor vascularisation on survival of patients with advanced ovarian carcinoma.** *Histol Histopathol* 2009, **24**:425–435.
42. Konda VJA, Hart J, Lin S, Tretiakova M, Gordon IO, Campbell L, Kulkarni A, Bissonnette M, Seewald S, Waxman I: **Evaluation of microvascular density in Barrett's associated neoplasia.** *Modern Pathology* 2013, **26**:125–130.
43. Szöke T, Kayser K, Trojan I, Kayser G, Furak J, Tiszlavicz L, Baumhäkel JD, Gabius HJ: **The role of microvascularization and growth/adhesion-regulatory lectins in the prognosis of non-small cell lung cancer in stage II.** *European Journal of Cardio-Thoracic Surgery* 2007, **31**(5):783–787, [<http://ejcts.oxfordjournals.org/content/31/5/783.abstract>].

Figures

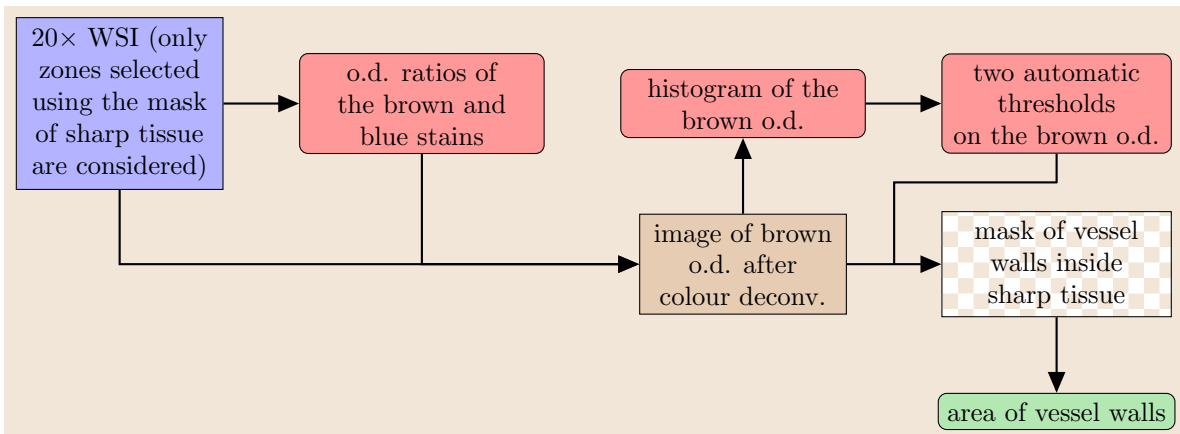
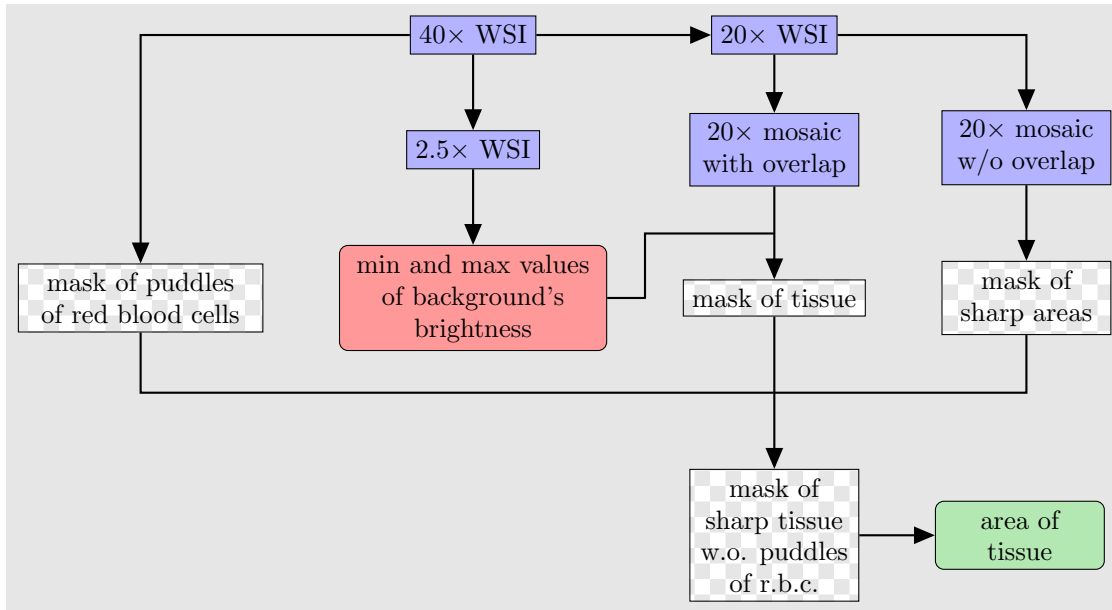


Figure 1 - Overview of the whole method of selection of sharp tissue (top) and of vessel walls inside sharp tissue (bottom)

The blue boxes represent real, full colour images; the checkerboard boxes represent masks (black-on-white images resulting from the selection of objects); the red boxes represent automatically determined quantitative parameters; the brown box represents the image of the brown optical densities of pixels of the original 20x image; the green boxes represent the final measured quantities.

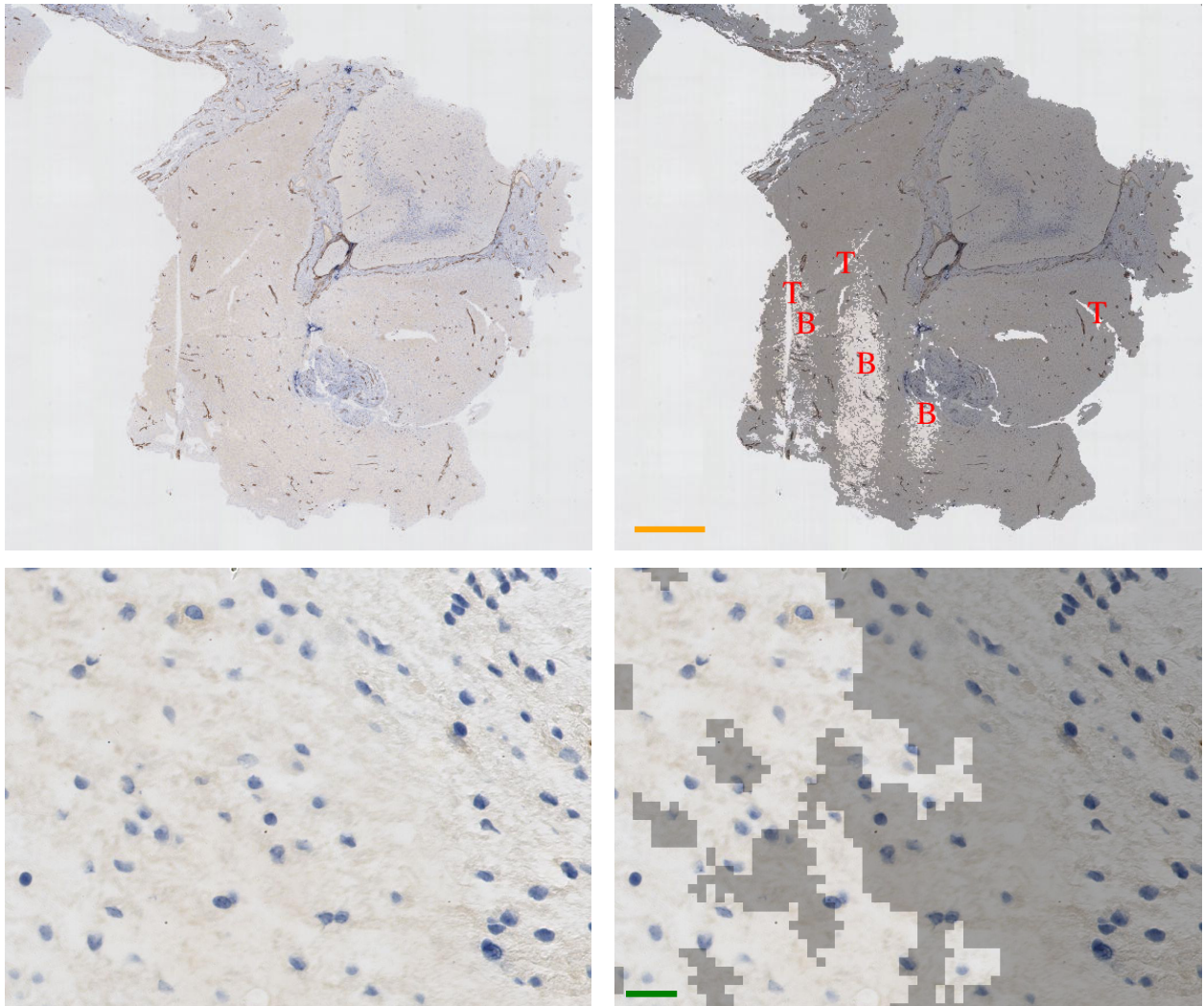


Figure 2 - Example of a determination of tissue without blur.

Top left: excerpt of the original image (one of our WSI). **Top right:** the mask (logical and combination of the mask of tissue and of the mask of sharp regions) is superimposed onto the WSI. Only regions considered, after our method, as sharp tissue are shaded. One can see in particular that tears inside the tissue are properly not counted as tissue (some of them are marked 'T'). Blurred regions (some of them are marked 'B') tend to form three vertical bands because of the way the image was acquired by the scanner. They will be excluded from the quantification process. Orange scale bar = 1 mm. **Bottom left:** detail of the top right image at the boundary of a blurred region. **Bottom right:** the mask of sharp regions is superimposed onto the detail of the WSI shown on the bottom left. One sees the transition between “fully blurred”, on the left-hand side of the image, to “fully sharp”, on the right-hand side of the image. Green scale bar = 20 microns.

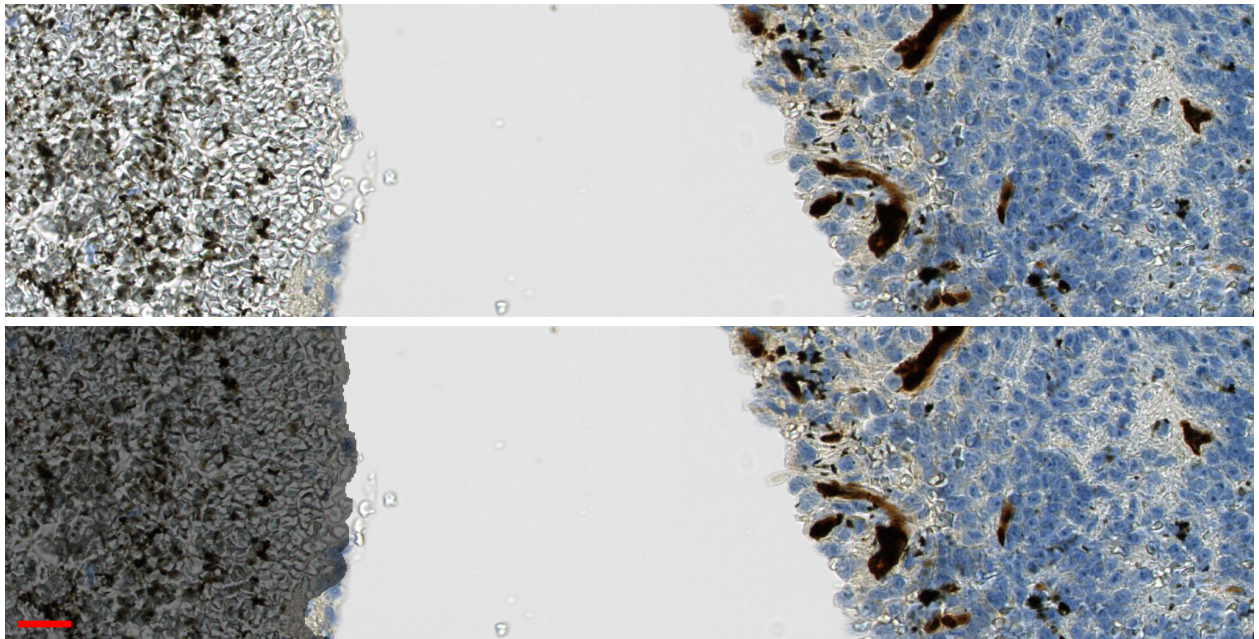


Figure 3 - Example of a determination of large puddles of red blood cells.

Top: original image (excerpt of one of our WSI). **Bottom:** the same image, over which the mask of the large puddles of red blood cells was superimposed. Scale bar = 20 microns.

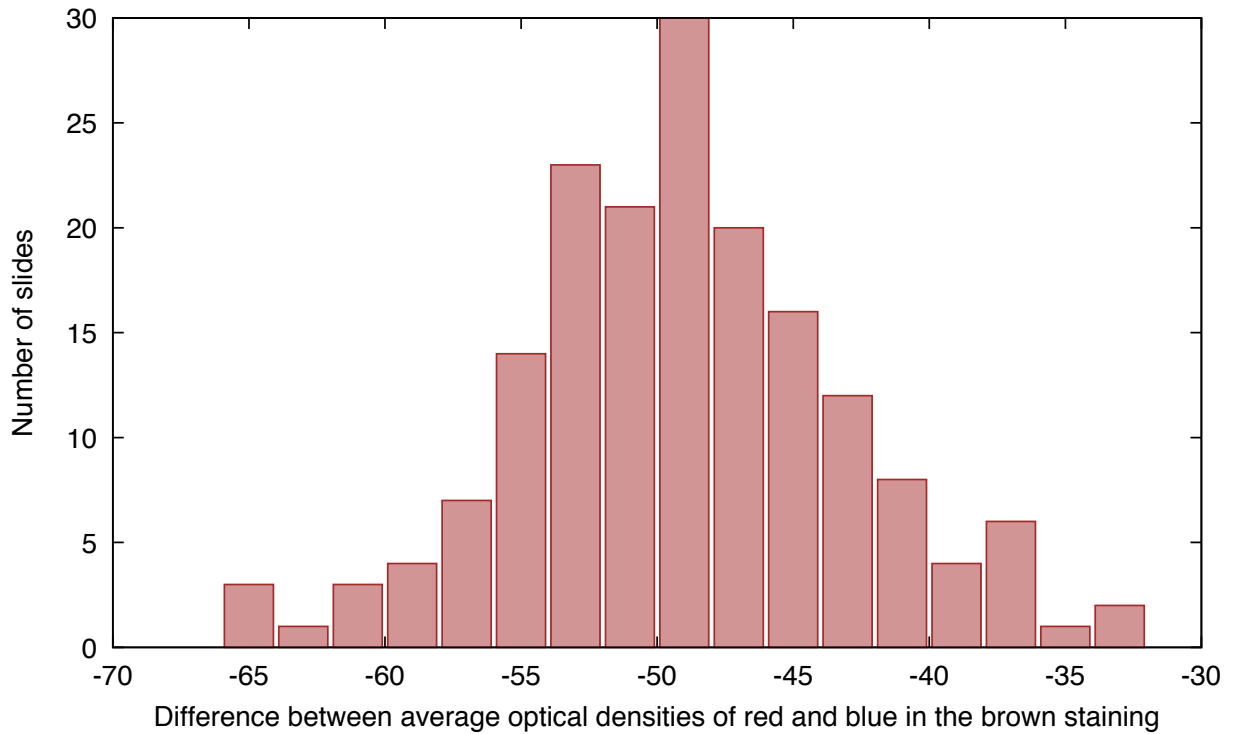


Figure 4 - Slide-to-slide variability of the optical densities of the brown staining.

For each WSI, after calibrating the optical densities in the red, green and blue channels of the brown (CD34) staining as defined in [36] according to the procedure described in the main text, we subtracted the blue optical density to the red optical density — let's call this difference Δ . This histogram shows the distribution of the values of Δ over the 186 WSI. One can see that there is a strong variability, which prevents one to use a single set of optical densities to perform colour deconvolution on all WSI.

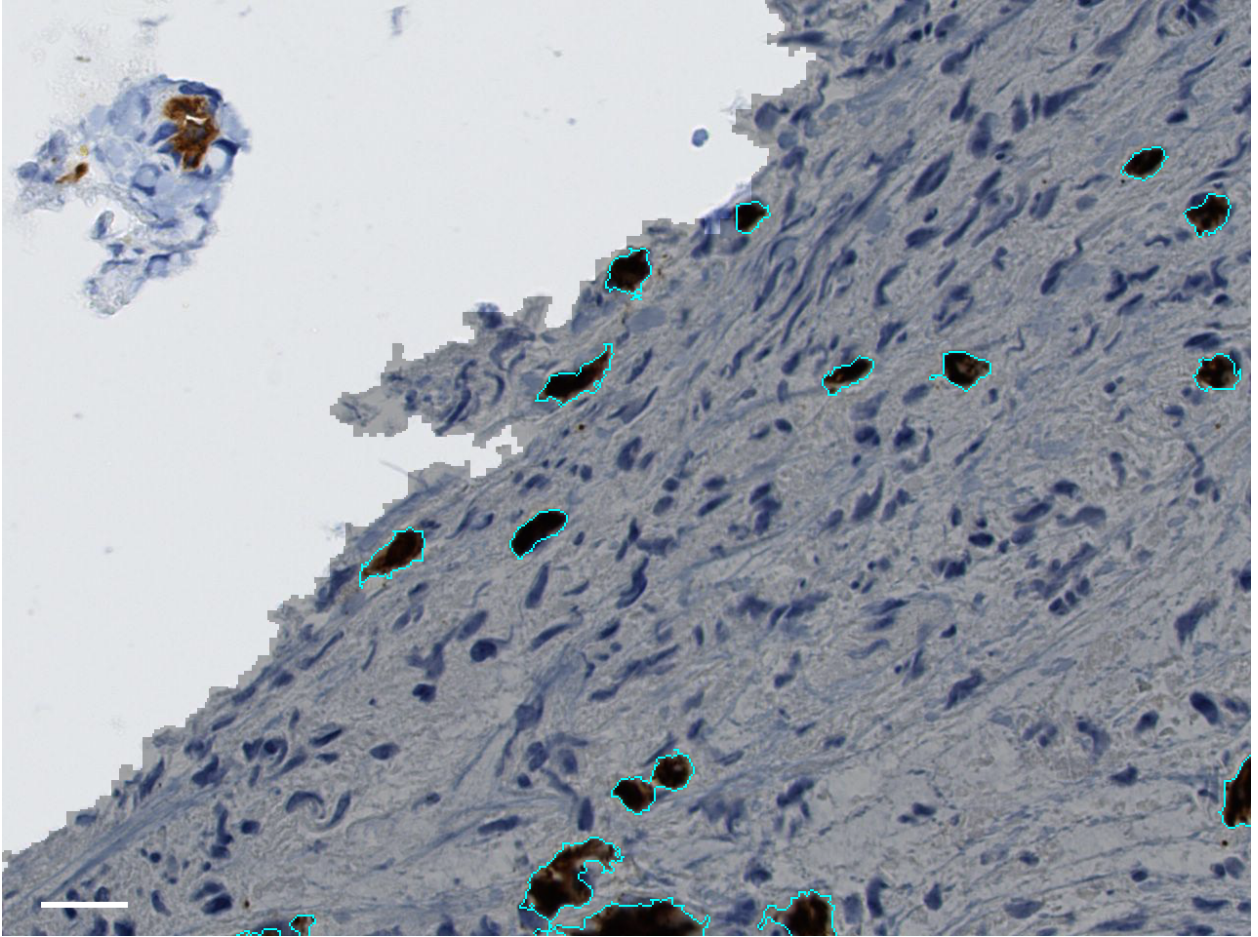


Figure 5 - Example of a segmentation of tissue and vessel walls (detail).

On this excerpt of a WSI at resolution 40 \times , the final result of the segmentation by our method is shown. The areas considered as sharp tissue are shaded, and the areas inside sharp tissue considered as vessel walls on the basis of the CD34 immunostaining are contoured in cyan. Scale bar = 20 microns.

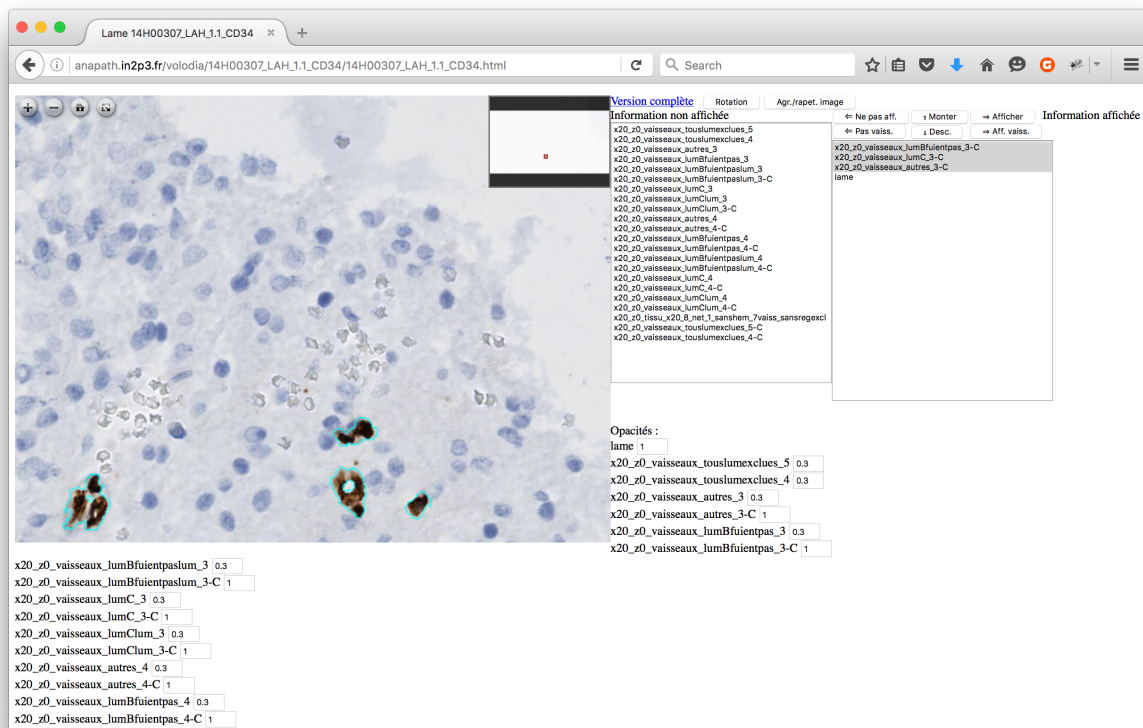


Figure 6 - A typical session of quality control of the segmentation in a standard web browser

The user is viewing, in the window of his JavaScript-capable web browser (here, Firefox), a detail of one of the whole slide images at full resolution (40×), on which he has superimposed the contours of the vessel walls (displayed in cyan on top of the slide). He can interactively add/remove contours and masks (displayed by shading the slide) to/from the list of displayed information, zoom in and out and drag the slide to explore it with his mouse.

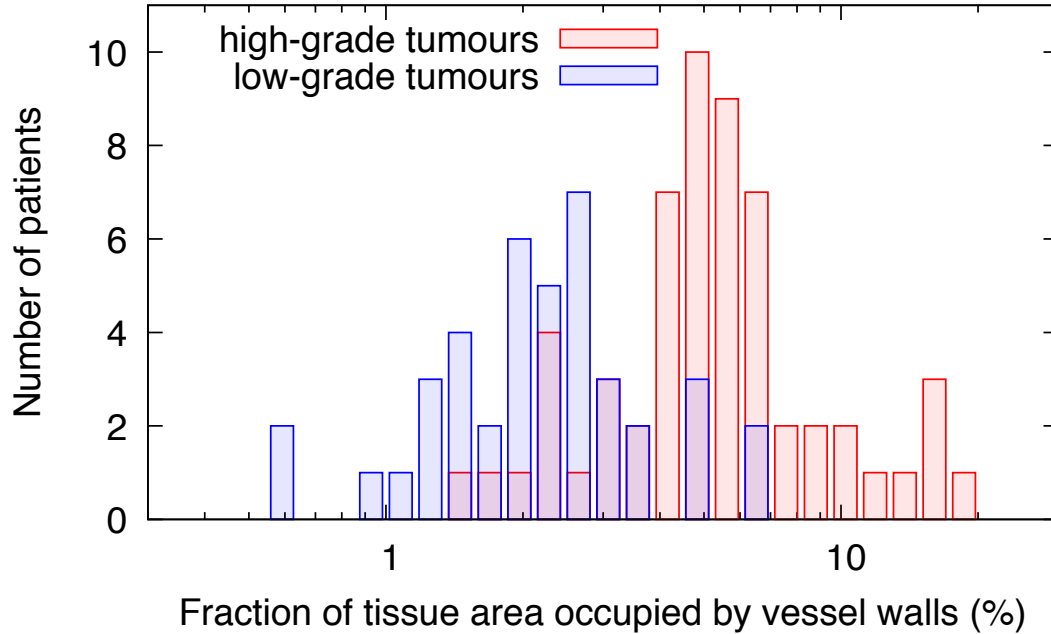


Figure 7 - Distribution of the density of microvessels in the tissue for patients suffering a high-grade resp. low-grade tumour

The red (resp. blue) histogram shows the distribution of the microvascular density (fraction of sharp tissue area covered with CD34-stained vessel walls) measured by our method on the WSI of samples from high-grade (resp. low-grade) tumours. Although the two histograms (here shown in log-lin scale) are relatively broad, there is a clear distinction between the typical microvascular densities of low- and high-grade tumours. We argue that the measurement uncertainties of the microvascular density (see Discussion in the main text) are much lower than the difference between these typical values.

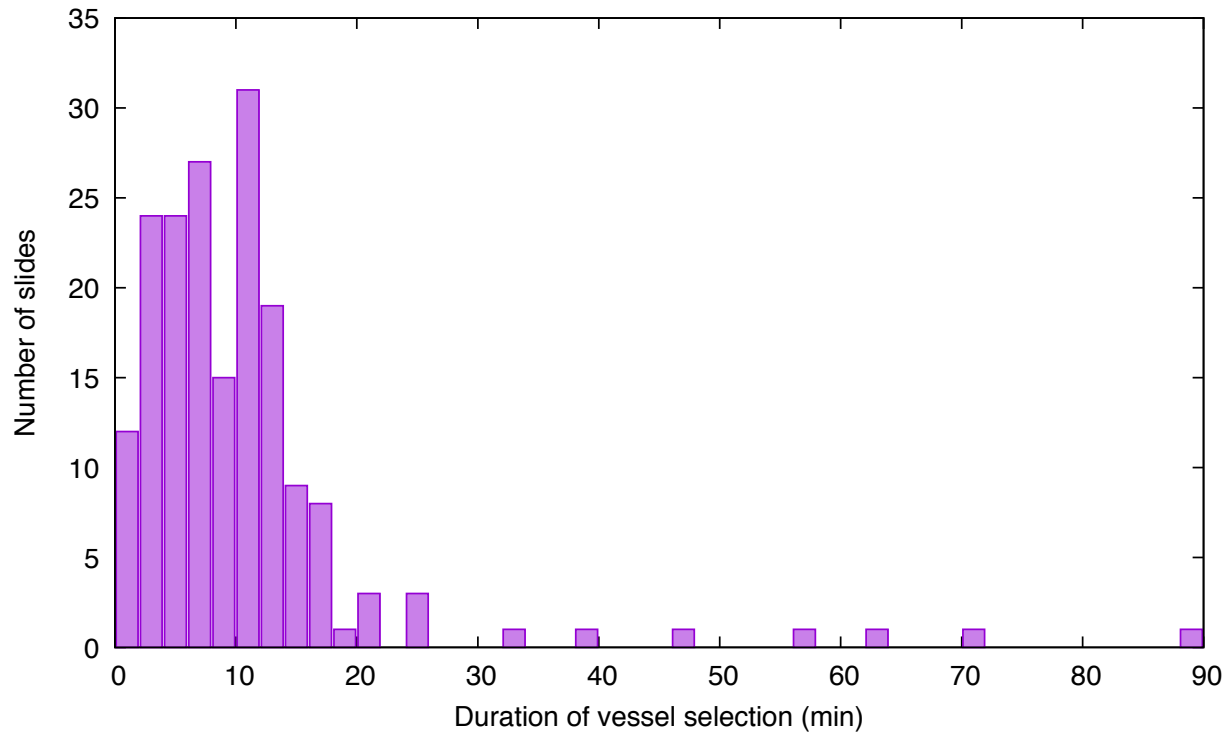


Figure 8 - Distribution of the duration of the process of colour deconvolution and vessel wall selection of all WSI on our Mac mini computer

Although a few WSI can request anomalously large treatment times, a vast majority of them are treated in less than 15 min on the rather modest computer we used for this study.

Tables

Table 1 - Types and locations of the 129 paediatric brain tumours in our study

Posterior fossa	85	Thalamus	10	Hemispheres	34
Pilocytic astrocytoma	29	Pilocytic astrocytoma	5	Atypical teratoid rhabdoid tumour	5
Grade I ganglioglioma	4			Grade I ganglioglioma	13
Medulloblastoma	33	Grade III astrocytoma	3	Pleomorphic xanthoastrocytoma	1
Grade III ependymoma	9			Grade III ependymoma	3
Grade III ganglioglioma	1			Grade III ganglioglioma	3
Other embryonal tumors	7	Glioblastoma	2	Glioblastoma	7
Glioma not otherwise spec.	1			Glioma not otherwise specified	1
Hemangioblastoma	1			Pleomorphic xanthoastrocytoma with anaplastic features	1